Quantitative assessment of flow velocity-estimation algorithms for optical Doppler tomography imaging

Daqing Piao, Linda L. Otis, Niloy K. Dutta, and Quing Zhu

We present a quantitative comparison of three categories of velocity estimation algorithms, inclu centroid techniques (the adaptive centroid technique and the weighted centroid technique), the sli window filtering technique, and correlation techniques (autocorrelation and cross correlation). introduce, among these five algorithms, two new algorithms: weighted centroid and sliding-wir filtering. Simulations and *in vivo* blood flow data are used to assess the velocity estimation accur of these algorithms. These comparisons demonstrate that the sliding-window filtering techniq superior to the other techniques in terms of velocity estimation accuracy and robustness to n © 2002 Optical Society of America

OCIS codes: 170.4500, 170.1650, 100.2000, 170.3880.

1. Introduction

Optical Doppler tomography (ODT) is a functional extension of optical coherence tomography (OCT) and it permits measurements of depth-resolved blood flow in turbid biological media.[1-9] OCT utilizes the amplitude of the interference signal between a sample and a scanning reference mirror to provide the morphology structure image of the biology tissue,[10] while ODT realizes phase-sensitive detection of the interference signal by tracking Doppler shifts arising from the moving scatterers inside the tissue. Recently, several research groups have investigated different velocity estimation algorithms, which can be classified into three major categories as a short-time Fourier-transform[1-4] method, a filtering method[6] and a Hilbert-transform[7,8] method. The short-time Fourier-transform method extracts local Doppler shifts by measuring the spectrum centroid of the interference signal. However, it is shown in Ref. 5 that the spectrum centroid gives rise to unavoidable velocity-estimation inaccuracies when scatterer distributions in the flow field fluctuate. The adaptive

short-time Fourier-transform technique introdu in Ref. 5 calculates the spectrum centroid only frequencies distributed symmetrically around spectrum peak within the Doppler bandwidth, has achieved high-fidelity depth-resolved measu ments of velocities in turbid media. The filter method introduced in Ref. 6 is implemented by herent demodulation at multiple frequencies follow by low-pass filtering, and it partially accommoda the broadband requirement of ODT. The Hilbe transform method or cross-correlation method cal lates a cross correlation between sequential A-sc lines and estimates velocity changes from the ph of the cross-correlation function.[7,8] The auth have reported high sensitivity of the method in es mating slow-moving blood flows.

In this paper we present the first quantitative cc parison of three categories of velocity-estimation gorithms, including centroid techniques (t adaptive centroid technique[5] and the weighted ce troid technique), the sliding-window filtering tec nique, and correlation techniques (autocorrelatio and cross correlation[7,8]). The comparisons ; based on estimation accuracy of the flow veloci The weighted centroid and sliding-window filteri algorithms are, to our knowledge, first introduced this paper. The autocorrelation technique has lo been used in ultrasound blood velocity measu ment.[11] In ultrasound, it calculates the normaliz mean frequency shifts from successive pulses usi the complex autocorrelation function of lag one in t depth direction. Because of its simplicity in comp tation and consequently in hardware implement

D. Piao (piao@engr.uconn.edu) and Q. Zhu (zhu@engr.uconn.edu) are with the Department of Electrical and Computer Engineering, University of Connecticut, Storrs, Connecticut 06269-2157. L. L. Otis is with the School of Dental Medicine, University of Pennsylvania, Philadelphia, Pennsylvania 19104-6003. N. K. Dutta is with the Department of Physics, University of Connecticut, Storrs, Connecticut 06269-3046.

tion, most ultrasound scanners use this method. Recently, the autocorrelation technique has been implemented in ODT.[12]

2. Velocity-Estimation Algorithms and Relevant Considerations

In conventional OCT, the detected interference signal is, in general, filtered with a narrow bandpass filter and Hilbert transformed to obtain the complex amplitude of the backscattered light. The narrow bandpass filter provides a high signal-to-noise ratio (SNR) and averaging is not necessary. In ODT, however, the detection of flow-induced frequency shift requires a bandpass filtering of a broader bandwidth, resulting in a significant degradation of the SNR in the B-scan image and a lower dynamic range in the corresponding flow image.[6] Averaging, therefore, is necessary in ODT to improve the SNR and to pursue high-fidelity flow-velocity estimation.

By taking into account the averaging, we express the detected two-dimensional (2-D) interference signal after Hilbert transformation as

$$\tilde{z}_{k,i}(t) = |\tilde{z}_{k,i}(t)|\exp(j\omega t), \qquad (1)$$

where t is the time argument along the depth scanning direction, k represents the lateral dimension of the kth A line, i is the index of the repeated A-line measurements, and ω is the angular frequency of signal reflected from the target. For a stationary target, $\omega = \omega_0 = 2\pi f_0$, where f_0 is the fundamental modulation frequency generated by the reference arm. For a moving scatterer, $\omega = \omega_0 \pm \omega_s = 2\pi(f_0 \pm f_s)$, where f_s is the Doppler shift generated by the moving scatterer. The velocity of the moving scatterer v_s is given as[5,13]

$$v_s = \frac{\omega_s}{\omega_0}\frac{c}{2\mu_g \cos\theta}, \qquad (2)$$

where c is the velocity of light in free space, μ_g is the refractive index of the sample, and θ is the angle between the light beam and the scatterer velocity vector. Because the flow velocity v_s is proportional to the Doppler shift ω_s, we will estimate ω_s or equivalently $\omega = \omega_0 + \omega_s$ throughout this paper.

A. Fourier-Transform Techniques

1. Centroid Techniques

Denoting the power spectrum of $\tilde{z}_{k,i}(t)$ with $P_{k,i}(\omega)$, we express the mean angular frequency, or the centroid of the power spectrum, as[14]

$$\bar{\omega}_{k,i} = \frac{\int_{-\infty}^{\infty} \omega P_{k,i}(\omega)\mathrm{d}\omega}{\int_{-\infty}^{\infty} P_{k,i}(\omega)\mathrm{d}\omega}. \qquad (3)$$

Because $\tilde{z}_{k,i}(t)$ represents a signal whose spectral contents change with time whenever there is a moving

scatterer in the local region, the local Doppler spectra could be obtained by applying a short-time Fourier transform (STFT) to the time-dependent detected signal.[4] If we use $\mathrm{STFT}_{k,i}(t_n, \omega)$ to represent the discrete STFT of the sampled interferometric signal $\tilde{z}_{k,i}(t_n)$, where $t_n = nt_s$ and t_s is the sampling interval, the local power spectra is given by

$$P^n_{k,i}(\omega) = \mathrm{STFT}_{k,i}(t_n, \omega)\overline{\mathrm{STFT}_{k,i}(t_n, \omega)}, \qquad (4)$$

where $\overline{\mathrm{STFT}_{k,i}(t_n, \omega)}$ is the complex conjugate of $\mathrm{STFT}_{k,i}(t_n, \omega)$. The conventional centroid technique estimates the centroid of a local Doppler spectrum by

$$\bar{\omega}_{k,i}(n) = \frac{\int_{-\infty}^{\infty} \omega P^n_{k,i}(\omega)\mathrm{d}\omega}{\int_{-\infty}^{\infty} P^n_{k,i}(\omega)\mathrm{d}\omega}. \qquad (5)$$

Because the noise power in the STFTs of segmented A lines is always positive and the centroid calculation integrates over signals as well as noise, the centroids of the STFTs always underestimate the true Doppler shifts.[5] In Ref. 5, it has been demonstrated that stochastic modifications of the Doppler spectrum by fluctuating scatterer distributions in the flow field give rise to unavoidable velocity-estimation inaccuracies.

2. Adaptive Centroid Technique

An adaptive centroid technique is introduced in Ref. 5, and it locates the Doppler spectral peak and calculates the centroid of the power only at frequencies distributed symmetrically around the peak within the Doppler bandwidth. The algorithm is given by

$$\bar{\omega}_{k,i}(n) = \frac{\int_{\omega_p-\Delta\omega/2}^{\omega_p+\Delta\omega/2} \omega P^n_{k,i}(\omega)\mathrm{d}\omega}{\int_{\omega_p-\Delta\omega/2}^{\omega_p+\Delta\omega/2} P^n_{k,i}(\omega)\mathrm{d}\omega}, \qquad (6)$$

where ω_p is the frequency corresponding to the maximum power in the spectrum, and $\Delta\omega$ is the Doppler bandwidth by the moving scatterer. This algorithm has shown significant improvement in the flow velocity-estimation accuracy over the centroid technique.

In this adaptive centroid algorithm, two parameters need to be carefully chosen. The first parameter is $\Delta\omega$, or the Doppler bandwidth caused by the moving scatterer in Equation (6). The full width at half-maximum (FWHM) of the Doppler spectrum is given as[5]

$$\Delta f = 2(V_0 - V_s)\Delta\nu/c \qquad (7)$$

where $\Delta\nu$ is the FWHM of the source power spectrum, V_0 is the equivalent reference mirror scanning speed, and V_s is the moving scatterer speed. Because the fundamental modulation frequency $f_0 = 2v_0V_0/c$,

where v_0 is the source center frequency, the ratio of $\Delta f / f_0$ can be approximated by $\Delta v / v_0$ as long as V_s is not too large compared with V_0. For STFT, each processing segment has typically 32 data points;[4] therefore, for typical light sources used in ODT with $\Delta v / v_0 \leq 5\%$, the integration of Eq. (6) is restricted to 1 or 2 points in the neighborhood of the power spectrum peak. We have chosen a total of 3 points in the neighborhood of the power spectrum peak among the 32 interpolated spectrum points when we implement the adaptive centroid calculation.

The second parameter that affects the outcome of this adaptive centroid algorithm is the noise-recognition level. In Ref. 5, the signal was considered noisy if the ratio of the average spectral density of the complete STFT over the spectral density within a bandwidth Δf around the peak was greater than a certain threshold T_0, in which case the traditional centroid algorithm was used for velocity estimation. Based on our study, we choose the optimum noise-recognition level as 0.6, which is very close to the value of 0.67 used in Ref. 5.

3. Weighted Centroid Algorithm

In this paper, we introduce a weighted centroid algorithm, which is an extension of the conventional centroid method. The algorithm is given by

$$\bar{\omega}_{k,i}(n) = \frac{\displaystyle\int_{-\infty}^{\infty} \omega [P^n_{k,i}(\omega)]^\xi d\omega}{\displaystyle\int_{-\infty}^{\infty} [P^n_{k,i}(\omega)]^\xi d\omega}, \qquad (8)$$

where a positive integer ξ is introduced as the weight of the spectra to emphasize the frequency component corresponding to the peak power in the spectra. If ξ is too small, this algorithm will underestimate the Doppler shifts as the conventional centroid technique does. However, if ξ is too big, the weighted spectra will be narrowed toward locations in which spectra each local maximum values. In this case the weighted centroid algorithm is similar to the algorithm that finds peaks of spectra and is known as being sensitive to noise. To obtain the optimum value of ξ, we studied the estimation accuracies of different ξ values using simulated data at various SNRs. The optimum value of ξ is found to be 6. It is shown in this paper that the newly introduced weighted centroid technique performs slightly better than the adaptive centroid technique in terms of velocity-estimation accuracy and robustness to noise.

Sliding-Window Filtering Technique

In this paper, we introduce what is to our knowledge a new filtering method by directly mapping the frequency shift at each pixel by using digital bandpass filtering. We assume that the local power spectrum $P^n_{k,i}(\omega)$ of the detected signal $\tilde{z}_{k,i}(t_n)$ has a peak at $\omega_p = \omega_0 + \omega_s$. If $\tilde{z}_{k,i}(t_n)$ is digitally bandpass filtered with a sliding filter window (ω_1, ω_2), the filtered

$\tilde{z}_{k,i}(t_n)$ will have a maximum power when the condition $\omega_1 < \omega_p < \omega_2$ is satisfied or, in other words, spectrum distributed around the peak falls in filtering window. The relative position of the sliding filter window to the fundamental frequency, $(\omega_1 + \omega_2)/2 - \omega_0$, represents the frequency shift of the scatterers.

The filtering window (ω_1, ω_2) determines the velocity resolution of this algorithm, and a better resolution requires a narrower filtering window. However, a robust estimate of the velocity requires broader filtering window. A compromise between velocity resolution and robustness to noise has been achieved by using a second-order Chebyshev filter the first kind, which has a bandwidth of $\pi/32$ and be slid from 0 to π in 32 steps. The velocity resolution achieved is at the same order as that of centroid techniques. It is demonstrated in this paper that using this filter window, the newly introduced sliding-window filtering technique is superior to the centroid techniques in terms of accuracy velocity estimation and robustness to noise.

C. Correlation Techniques

1. Autocorrelation Technique

The complex autocorrelation function $R^n_{k,i}(\tau)$ $\tilde{z}_{k,i}(t_n)$ is represented as

$$R^n_{k,i}(\tau) = \int_{t_n - Nt_s}^{t_n} \tilde{z}_{k,i}(t + \tau) \times \overline{\tilde{z}_{k,i}(t)} dt,$$

where Nt_s is the time duration of integration. Because the autocorrelation function can be represented by

$$R^n_{k,i}(\tau) = |R^n_{k,i}(\tau)| \exp[j \phi_{k,i}^n(\tau)],$$

the mean frequency $\bar{\omega}$ can be approximated as[11]

$$\begin{aligned}
\bar{\omega}_{k,i}(n) &= \dot{\phi}^n_{k,i}(0) \\
&\approx \frac{\phi^n_{k,i}(\Delta T)}{\Delta T} \\
&\approx \frac{1}{\Delta T} \tan^{-1}\left\{ \frac{\mathrm{Im}[R^n_{k,i}(\Delta T)]}{\mathrm{Re}[R^n_{k,i}(\Delta T)]} \right\},
\end{aligned}$$

where ΔT denotes the temporal lag, and $\dot{\phi}^n_{k,i}(0)$ is the derivative of $\phi^n_{k,i}$ at $\Delta T = 0$.

2. Cross-correlation Technique

In the cross-correlation technique, the phase change of the cross-correlation function of sequential A-scan lines are used to estimate the mean frequency. The cross correlation of lag 1 is given by

$$C^n_{k,i}(T) = \int_{t_n - NT}^{t_n} \tilde{Z}_{k,i}(t + T) \times \overline{\tilde{Z}_{k+1,i}(t)} dt,$$
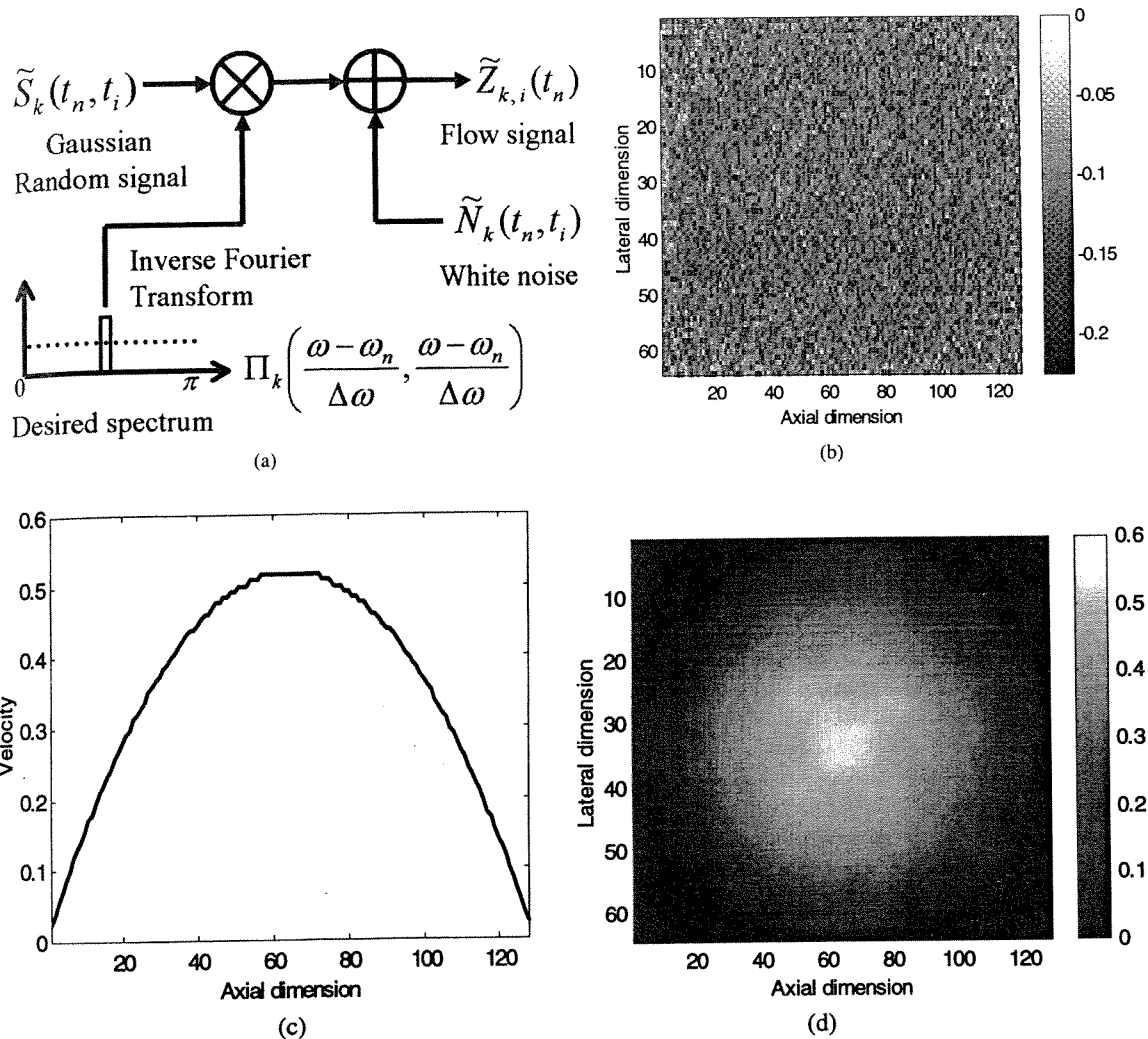
Fig. 1. Laminar flow signal simulation. (a) Schematic of the simulation model, (b) amplitude image of simulated 2-D flow signal, (c) 1-D velocity profile pattern of the simulated flow signal, (d) 2-D velocity image of the simulated flow signal.

where T is the time interval between sequential A scans. Because the cross-correlation function can be represented as

$$C^n_{k,i}(\tau) = |C^n_{k,i}(\tau)|\exp[j\phi^n_{k,i}(\tau)], \qquad (13)$$

the mean angular frequency $\bar{\omega}$ is given by[8]

$$\bar{\omega}_{k,i}(n) \approx \frac{\phi^n_{k,i}(T)}{T} \approx \frac{1}{T}\tan^{-1}\left\{\frac{\mathrm{Im}[C^n_{k,i}(T)]}{\mathrm{Re}[C^n_{k,i}(T)]}\right\}. \quad (14)$$

3. Laminar Flow Simulation Model

To quantitatively assess the velocity-estimation accuracy of the above-mentioned estimation algorithms, we have simulated blood-flow signals with different SNRs. In the simulation, we chose laminar flow as a typical blood-flow profile and represent the velocity distribution $V(r)$ in a cylindrical conduit at radial position r as[1]

$$V(r) = \frac{d^2 \Delta p}{16\mu\Delta L}\left[1 - \left(\frac{2r}{d}\right)^2\right], \qquad (15)$$

where d is the internal diameter of the conduit, Δp is the pressure difference along a length ΔL of the conduit, and μ is the viscosity of the flowing fluid. Based on this parabolic velocity flow profile, we simulated 2-D laminar flow signals. The simulation model is illustrated in Fig. 1(a) and represented by

$$\tilde{Z}_{k,i}(t_n) = \tilde{S}_k(t_n, t_i) \otimes F^{-1}\left[\prod_k\left(\frac{\omega - \omega_n}{\Delta\omega}, \frac{\omega - \omega_n}{\Delta\omega}\right)\right] + \tilde{N}_k(t_n, t_i), \qquad (16)$$

where $t_n = nt_s$ as previous defined, and $t_i = it_s$. First, we generate a 2-D Gaussian random signal $\tilde{S}_k(t_n, t_i)$, which has a uniform spectrum. Second, a 2-D rectangular window function $\prod_k[(\omega - \omega_n)/\Delta\omega, (\omega - \omega_n)/\Delta\omega]$ is generated to simulate the desired spectrum with ω_n and $\Delta\omega$ representing the center frequency and spectrum bandwidth of the Doppler shift, respectively. Third, $\tilde{S}_k(t_n, t_i)$ is convolved with the inverse Fourier transform of $\prod_k[(\omega - \omega_n)/\Delta\omega, (\omega - \omega_n)/\Delta\omega]$ to produce a signal with the desired spectrum. Finally, an additive 2-D white noise
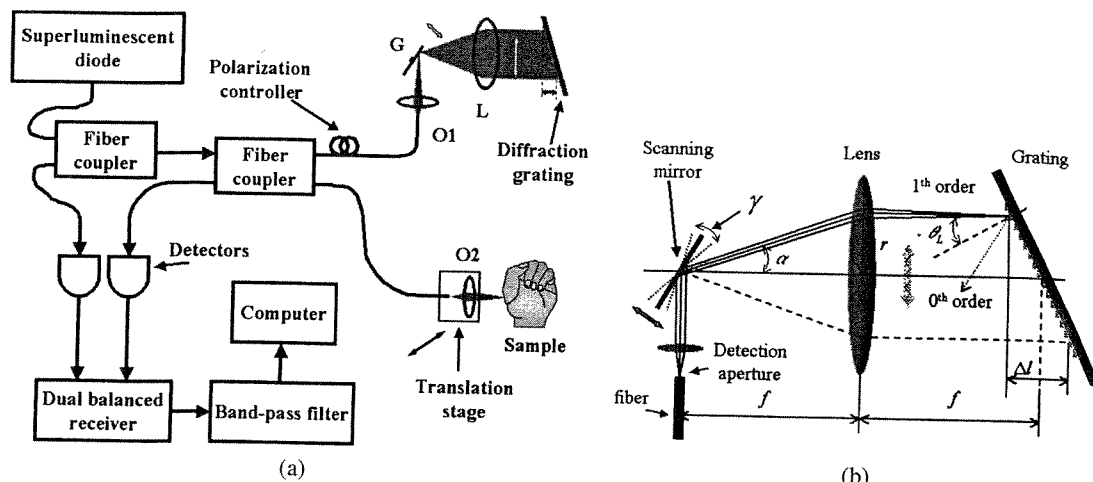
Fig. 2. (a) Schematic of the ODT system: O1, microscope objective lens; O2, GRIN lens; G, galvanometer; L, achromatic le: Illustration of scanning optical delay line by Littrow-mounting of diffraction grating: f, focal length; γ, the total rotation angl mirror; α, the divergence angle of the reflected light from the lens axis; r, the displacement of light from the lens axis at the surfac lens; θ_L, Littrow angle; Δl, the resulting optical delay.

$\tilde{N}_k(t_n, t_i)$ is introduced to the generated signal to account for the noise environment in the actual flow measurement. The SNR is controlled to facilitate the evaluation of the performance of different algorithms. We further segment the generated data of dimension 2048 × 512 to 2048 × 8 × 64, which corresponds to 2048 points in one A line (depth direction), 8 sequential A lines for averaging at one lateral step, and 64 lateral steps. These data dimensions of $\max(n) = 2048$, $\max(i) = 8$, and $\max(k) = 64$ are the same as that obtained experimentally, which will be reported in the following section. For each A-line signal, 16 data points correspond to one image pixel, which results in an image dimension of 128 (axial) × 64 (lateral). In the actual algorithm processing, a typical 50% overlapping is implemented, so for each pixel, 32 data points are actually processed. Figure 1(b) shows an amplitude image of simulated 2-D signals. The signal represents a laminar flow in a cylindrical conduit. Because SNRs of with/without flow regions are set to be equal, the structural cross-sectional image of flowing medium is hardly visible. Figure 1(d) is the corresponding 2-D laminar flow image generated with the model, and Fig. 1(c) represents a one-dimensional laminar pattern in any direction of the flow image in Fig. 1(d).

4. Optical Doppler Tomography Experimental System

The schematic of our ODT system is shown in Fig. 2(a). This ODT system is a typical balanced setup configured with one 1 × 2 and one 2 × 2 fiber couplers. A superluminescent diode with an emitting wavelength centered at 1300 nm and a spectral width of 40 nm is used as the low coherence source. The 3 dB coherence length is calculated and measured to be 18.6 μm and 19.0 μm respectively, and the output power is 2.2 mW at an injection current of 195 mA. We employed a new scanning optical-delay line based on a Littrow mounting of the diffraction grating at

the reference arm. The principle of this Lit mounting scanning optical-delay line is illustra Fig. 2(b). The reference light is incident at t] tation axis of a scanning mirror G (driven by ; nometer), and the rotation axis is aligned to be ; focal point of an achromatic lens L. With the the sector scanning by the dithering mirror is t lated to a spatially parallel scanning upon a p reflection grating. The grating is mounted ii trow angle, in which the light incident on the gr will be reflected back exactly along the incident path, and the optical path difference between cent beams turns out to be the optical delay. total scan range Δl is given by

$$\Delta l = 2f \tan(\theta_L)\tan(\gamma),$$

where f is the focal length of the lens, θ_L is the Lit angle of grating for the desired wavelength, γ i total rotation range of the mirror. At a small ; of mirror rotation, $\gamma(t) = \Gamma t$, where Γ is the mi scanning coefficient[15] the total scan range Δl ca simplified as

$$\Delta l = 2f\gamma \tan(\theta_L) = 2f\Gamma \tan(\theta_L)t.$$

The time derivative of the optical delay, $d_t(\Delta l) =$ tan θ_L, demonstrates the linearity of scanning constant Γ. When the light is incident at the a λ the mirror rotation, the scanning optical delay c; achieved without phase modulation. When the ror rotation axis is shifted a distance of δ, the p modulation introduced can be approximated by f_i $8\pi f_g\delta \sin(\gamma)/\lambda_0$, where f_g is the galvanometer s ning frequency, λ_0 is the center wavelength of source. In our ODT system, this Littrow-moun scanning delay line is adjusted to obtain a depth range of a maximum 3.25 mm and a phase mod tion frequency of 52.6 KHz for in vivo blood-flow aging when the mirror is driven under 64 Hz.
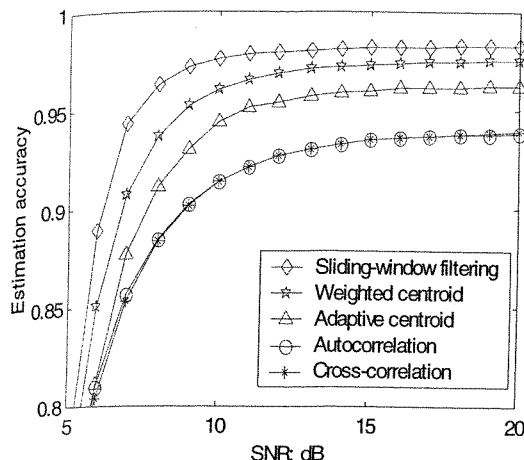
Fig. 3. Estimation accuracy as a function of the SNR of five estimation techniques.

sampling frequency is 262 KHz, and the bandwidth of receiving electronics can be varied from 10 KHz to 102.4 KHz.

In the sample arm, the light is focused with a gradient index lens of 0.3 numerical aperture. The lateral scanning is performed by use of a linear translation stage with a speed of 100 μm/s and submicron position accuracy. In one A line, there are 2048 data points, and a total of 512 sequential A lines are taken in 8 s. In the axial direction, 16 data points are averaged for one pixel; in the lateral direction, 8 sequential A lines are averaged for each lateral step. The lateral scanning range is 0.8 mm and the depth scanning range is 2.5 mm, resulting in an image resolution of 19.5 μm (axial) by 12.5 μm (lateral) for in vivo ODT.

5. Simulation and Experimental Results
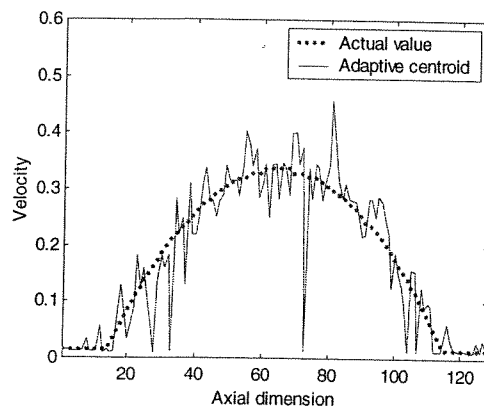
A. Simulations

All algorithms are tested from experimental data when no flow is present and they can accurately retrieve the modulation frequency. The accuracy of each algorithm is evaluated with the correlation coefficient between the estimated velocity profile and the actual profile that is available in simulation study. Figure 3 shows the estimation accuracy of each algorithm on simulated data as a function of SNR from 1 dB to 20 dB. The result for each algorithm at each SNR is an average of 5 data sets calculated independently by use of different additive white noises. At a higher SNR, e.g., greater than 15 dB, all algorithms provide a stable estimate of the velocity profiles with an estimation error of 2%, 3%, 4%, 7%, 7% for sliding-window filtering, weighted centroid, adaptive centroid, autocorrelation and cross-correlation techniques, respectively. At a lower SNR, e.g., less than 6 dB, there is significant difference in the performance of each algorithm. The sliding-window filtering technique and centroid techniques are superior to the correlation techniques, and the filtering technique is the best. It is clear

that over the entire SNR range that we have investigated, the sliding-window filtering is superior to other algorithms.

To visualize the performance of these algorithms and their robustness to noise, we present typical one-dimensional plots of the estimation results for each algorithm at SNR = 20 dB (Fig. 4) and SNR = 6 dB (Fig. 5). By comparing (a), (b) and (c) of Figs. 4 and 5, one can see that the estimation accuracies of the weighted centroid technique and the adaptive centroid technique are very similar but the weighted centroid is slightly more robust to noise. It is clearly shown that the sliding-window filtering technique outperforms the other techniques in terms of accuracy and the robustness to noise. By comparing (d) and (e) of Figs. 4 and 5, one can see that the correlation techniques provide a reasonably accurate estimate at high SNR and higher-velocity regions and a poor estimate at low SNR and/or low flow regions. The reason is that correlation techniques are more sensitive to local decorrelation of the flow field resulting from a low SNR or a high velocity gradient that is present at the low flow velocity region.[16]

B. In Vivo Blood-Flow Data

In vivo cross-sectional B-scan and blood-velocity images were obtained from a female volunteer who has a subepidermal area on her hand with aggregated small blood vessels (Fig. 6). Figure 6(a) is the B-scan image and Fig. 6(b) to 6(e) are the blood flow images estimated by using the adaptive centroid, the weighted centroid, the sliding-window filtering, and the autocorrelation technique, respectively. The fundamental modulation frequency is 52.6 KHz, and the ODT images are displayed in the range of 18 KHz to 82 KHz [see the color scales on the right-hand side of Fig. 6(b)–6(e)], which corresponds to a negative 34.6 KHz to a positive 29.4 KHz frequency shift. There are two regions with opposite colors, indicating the existence of two clusters of small blood vessels with opposite blood-flow directions. The four algorithms detect blood-flow signals of approximately similar volume and at approximately the same location. The sliding-window filtering algorithm is less noisy than the other algorithms. It is also shown that the autocorrelation method detects a larger volume, represented by the less sparse blood-flow area. This observation is supported by the simulations that have shown that correlation techniques tend to overestimate velocity at the low flow area when the SNR is low and, therefore, flatten out the difference between high- and low-velocity areas [see Fig. 5(d) and 5(e)]. Owing to a hardware limitation, we could not implement the cross-correlation method to our experimental data. The details are given in the next section. The SNR at the flow region is calculated to be approximately 10 dB. The performance of these 4 algorithms is consistent with that expected from Fig. 3 when the SNR is close to 10 dB.
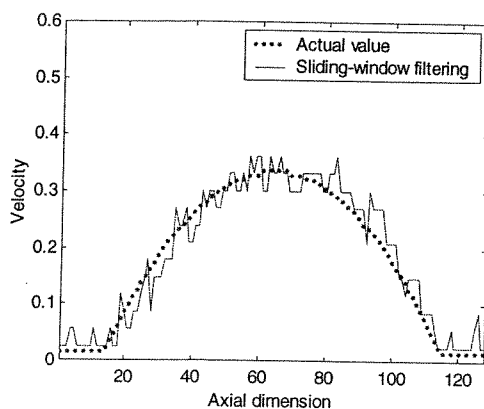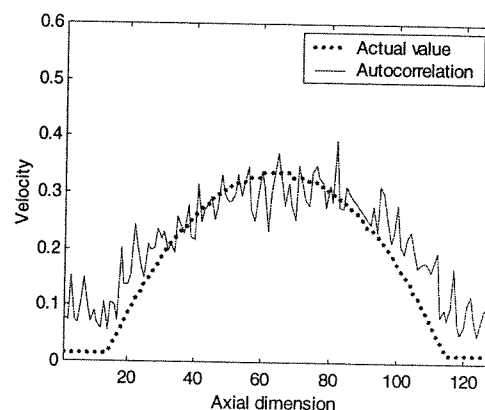
Adaptive centroid algorithm
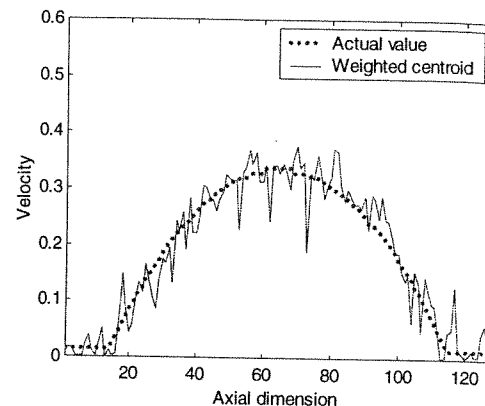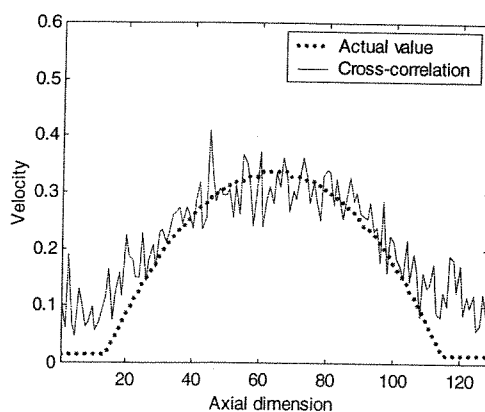
(a)

Weighted centroid algorithm

(b)

Sliding-window filtering algorithm

(c)

Autocorrelation algorithm

(d)

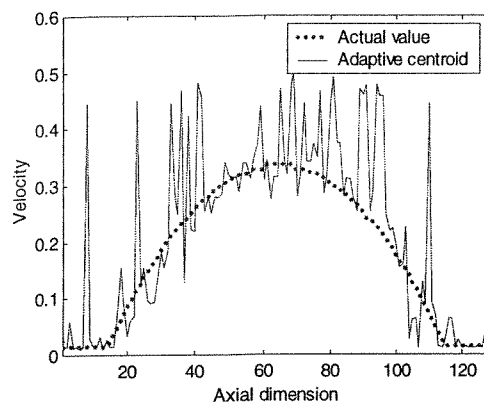Cross-correlation algorithm

(e)

Fig. 4. Comparison of simulated flow profile with the actual flow profile at a SNR = 20 dB. In each figure (a) adaptive centroid algorithm, (b) weighted centroid algorithm, (c) sliding-window filtering algorithm, (d) autocorrelation algorithm, (e) cross-correlation algorithm, the solid curve corresponds to the estimated velocity profile at $k = 13$ [k is the lateral dimension at Fig. 1(d)], and the dotted curve is the actual profile. The centroid techniques (a) and (b) provide accurate estimates, while they are sensitive to noise. The filtering technique (c) is more accurate and robust to noise. The correlation techniques (d) and (e) provide reasonably accurate velocity estimates at a high-velocity region but overestimate at low-flow velocity regions.

6. Discussion

In the autocorrelation technique, the mean frequency is estimated by the change in phase shift $\Delta\phi = \omega\Delta T = 2\pi f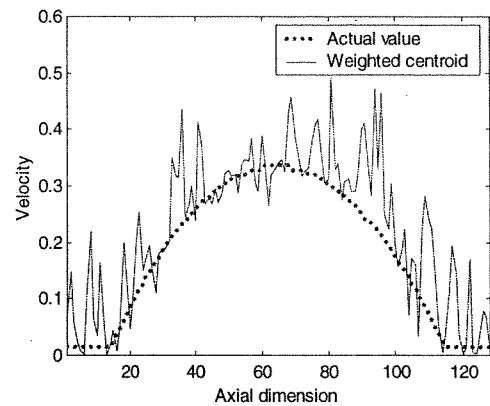\Delta T$ within a certain time delay ΔT. Therefore, the 2π phase ambiguity poses a tradeoff between velocity sensitivity and the maximum detectable locity. The maximum detectable velocity is then termined by $\omega_s = 2\pi/\Delta T \mp \omega_0$ depending on
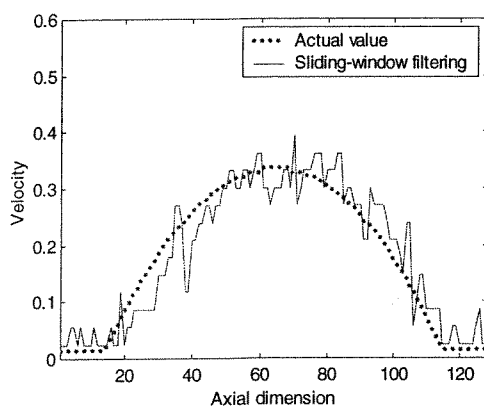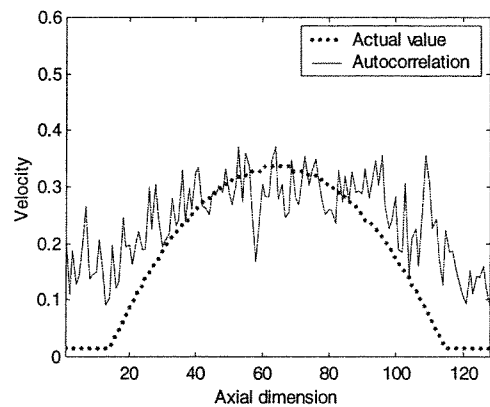
Adaptive centroid algorithm

(a)

Weighted centroid algorithm
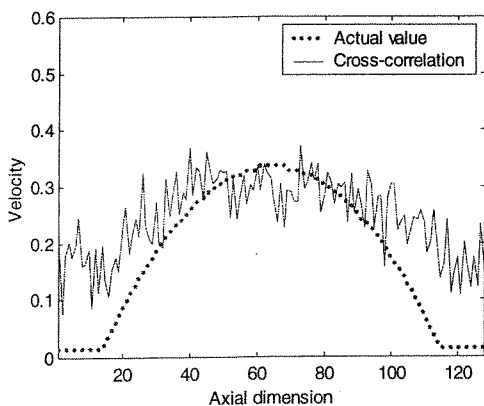
(b)

Sliding-window filtering algorithm

(c)

Autocorrelation algorithm

(d)

Cross-correlation algorithm

(e)

Fig. 5. Comparison of the simulated flow profile with the actual flow profile at a SNR = 6 dB. In each figure (a) adaptive centroid algorithm, (b) weighted centroid algorithm, (c) sliding-window filtering algorithm, (d) autocorrelation algorithm, (e) cross-correlation algorithm, the solid curve corresponds to the estimated velocity profile at $k = 13$ [k is the lateral dimension at Fig. 1(d)], and the dotted curve is the actual profile. Again, the weighed centroid algorithm is slightly less noisy than the adaptive centroid one while they have similar accuracy. The correlation techniques (d) and (e) show less accurate estimates in both high and low flow regions at this low SNR, but the techniques are free of noise spikes compared with the results of centroid techniques (a) and (b). Apparently, the filtering technique (c) has the best estimation at this low SNR in terms of accuracy and robustness to noise.

velocity direction ("−" for positive flow and "+" for negative flow). If demodulation is employed, then the maximum detectable velocity can be improved to $\omega_s = 2\pi/\Delta T$ regardless of the velocity direction. In biological blood-flow imaging, the highest detectable

velocity is as important as the velocity sensitivity. In the autocorrelation technique, ΔT is the sample interval in the axial direction and is small in general. Therefore a reasonably higher velocity can be detected even without demodulation. However, the
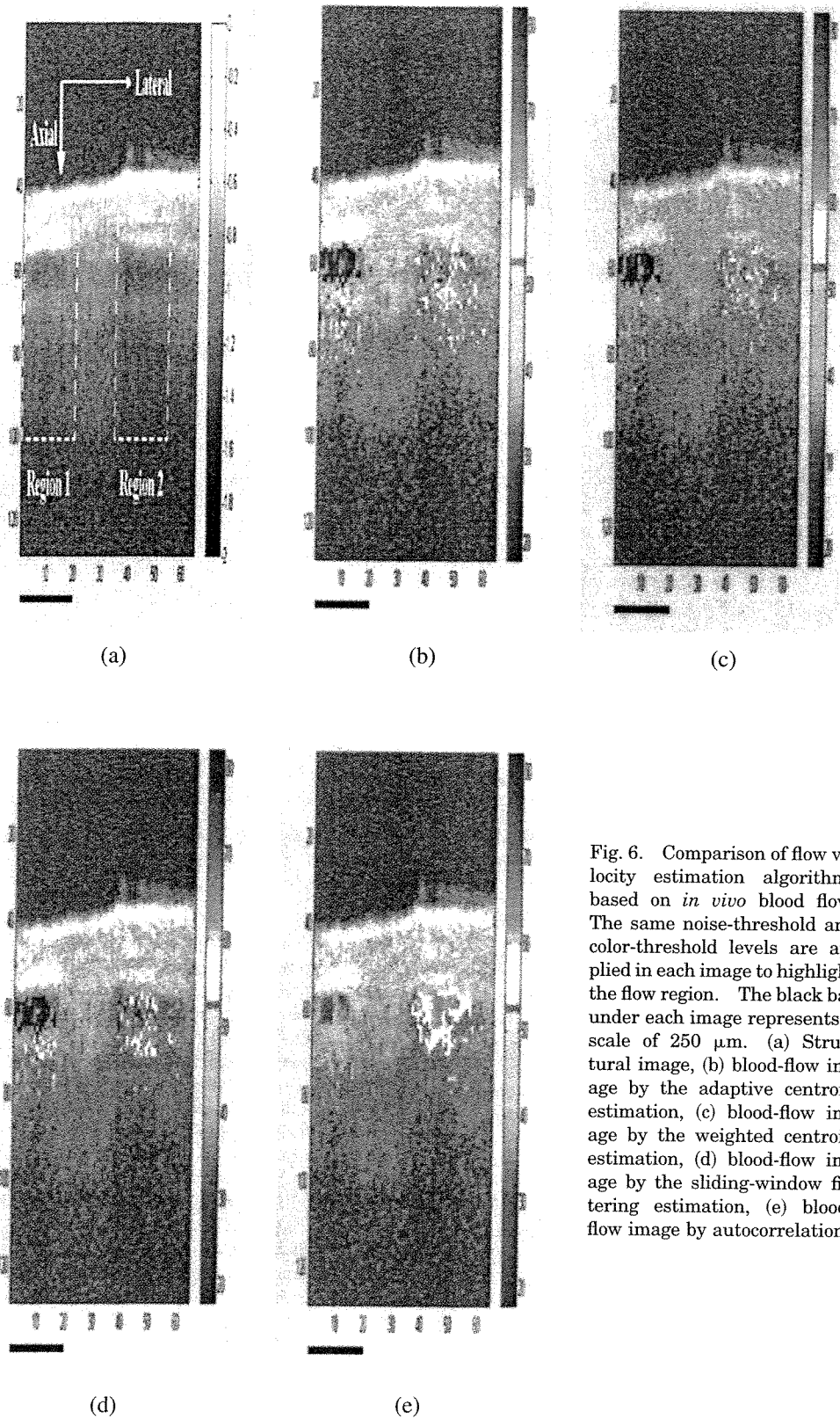
(a)

(b)

(c)

Fig. 6. Comparison of flow velocity estimation algorithms based on *in vivo* blood flow. The same noise-threshold and color-threshold levels are applied in each image to highlight the flow region. The black bar under each image represents a scale of 250 μm. (a) Structural image, (b) blood-flow image by the adaptive centroid estimation, (c) blood-flow image by the weighted centroid estimation, (d) blood-flow image by the sliding-window filtering estimation, (e) blood-flow image by autocorrelation.

(d)

(e)

cross-correlation technique, although demonstrating higher velocity sensitivity, poses a more strict requirement on the demodulation because the maxi-

mum frequency shift is limited to $\omega_s = 2\pi/T \mp$ where T is the interval between sequential A sc: T is much longer than (in general >100) the time

ΔT used in the autocorrelation technique. Thus the cross-correlation technique requires demodulation for avoiding 2π phase ambiguity, and achieves the high velocity sensitivity at the expense of the much lower maximum detectable velocity. In our ODT system, we used $\Delta T = 1/262144 \approx 2.81\ \mu s$ as the unit lag in autocorrelation estimation. Consequently, even without demodulation, the maximum detectable frequency can be as high as 200 KHz, if not limited by the Nyquist rate, for positive flow. However, because the time interval between sequential A scans of our system is $T = 1/64 \approx 15.6$ ms, the cross-correlation technique is unable to accurately detect the two flow regions without demodulation. Because our current OCT system does not have hardware demodulation capability, we have used software demodulation to implement the cross correlation. However, owing to the large T of our data-acquisition system, the 2π phase ambiguity still causes data wrapping in the velocity estimate. Therefore we have eliminated the comparison with the cross-correlation technique.

In this study, the dimension of the raw data corresponding to one cross-sectional image is 2048×512, and we used 8 sequential A lines for averaging at one lateral step, resulting in a final data dimension of $2048 \times 8 \times 64$. More averaging on sequential A lines certainly could give higher accuracy, however, this results in a longer data-acquisition time and consequently a larger computation load if lateral resolution is to be maintained. We have investigated the optimal averaging number using experimental data acquired from flow samples consisting of 0.25% intralipid solution. Using the correlation coefficient between the estimated flow profiles obtained with two consecutive average numbers, we found that the estimation accuracy increases from 0.93 to 0.98 as the averaging number increases from 2 to 8. Beyond 8, the increment in estimation accuracy is very small. Therefore, we have used 8 sequential A lines for the lateral averaging in processing simulation and experimental flow data.

The computation times for these 3 categories of algorithms we studied, namely the centroid techniques, the sliding-window filtering technique, and the correlation techniques, are 15 s, 60 s, and 106 s, respectively, for a data set of $2048 \times 8 \times 64$ using a Pentium III 800 MHz-based PC. We are currently implementing a digital signal processing based ODT system for real-time processing of ODT signals and the results will be reported in a future paper.

7. Summary

We presented a quantitative comparison among five flow-velocity algorithms, including three currently used methods in ODT and two newly implemented techniques. With simulations and in vivo blood-flow data we have demonstrated that the sliding-window filtering technique gives a consistently favorable performance over the adaptive centroid, the weighted centroid, and the correlation techniques in terms of estimation accuracy and robustness to noise. The centroid techniques are less robust to noise compared with the sliding-window filtering technique but are more accurate than the correlation techniques. The correlation techniques overestimate the velocity profile when the SNR is low and/or flow velocity is slow, but are free of spike noises.

References

1. X. J. Wang, T. E. Milner, and J. S. Nelson, "Characterization of fluid flow velocity by optical Doppler tomography," Opt. Lett. **20**, 1337–1339 (1995).
2. Z. P. Chen, T. E. Milner, D. Dave, and J. S. Nelson, "Optical Doppler tomographic imaging of fluid flow velocity in highly scattering media," Opt. Lett. **22**, 64–66 (1997).
3. Z. P. Chen, T. E. Milner, S. Srinivas, X. J. Wang, A. Malekafzali, M. J. C. van Germert, and J. S. Nelson, "Noninvasive imaging of in vivo blood flow velocity using optical Doppler tomography," Opt. Lett. **22, 14**, 1119–1121 (1997).
4. J. A. Izatt, M. D. Kulkarni, S. Yazdanfar, J. K. Barton, and A. J. Welch, "In vivo bi-directional color Doppler flow imaging of picoliter blood volumes using optical coherence tomography," Opt. Lett. **22**, 1439–1441 (1997).
5. M. D. Kulkarni, T. G. van Leeuwen, S. Yazdanfar, A. J. Welch, and J. A. Izatt, "Velocity-estimation accuracy and frame-rate limitations in color Doppler optical coherence tomography," Opt. Lett. **23**, 1057–1059 (1998).
6. T. G. van Leeuwen, M. D. Kulkarni, S. Yazdanfar, A. M. Rollins, and J. A. Izatt, "High-flow-velocity and shear-rate imaging by use of color Doppler optical coherence tomography," Opt. Lett. **24**, 1584–1586 (1999).
7. Y. H. Zhao, Z. P. Chen, C. Saxer, S. H. Xiang, J. F. de Boer, and J. S. Nelson, "Phase-resolved optical coherence tomography and optical Doppler tomography for imaging blood flow in human skin with fast scaning speed and high velocity sensitivity," Opt. Lett. **25**, 114–116 (2000).
8. Y. H. Zhao, Z. P. Chen, C. Saxer, Q. M. Shen, S. H. Xiang, J. F. de Boer, and J. S. Nelson, "Doppler standard deviation imaging for clinical monitoring of in vivo human skin blood flow," Opt. Lett. **25**, 1358–1360 (2000).
9. S. Yazdanfar, A. M. Rollins, and J. A. Izatt, "Imaging and velocimetry of the human retinal circulation with color Doppler optical coherence tomography," Opt. Lett. **25**, 1448–1450 (2000).
10. D. Huang, E. A. Swanson, C. P. Lin, J. S. Schuman, W. G. Stinson, W. Chang, M. R. Hee, T. Flotte, K. Gregory, C. A. Puliafito, and J. G. Fujimoto, "Optical coherence tomography," Science **254**, 1178–1181 (1991).
11. C. Kasai, K. Namekawa, A. Koyano, and R. Omoto, "Real-time two-dimensional blood flow imaging using an autocorrelation technique," IEEE Trans. Sonics Ultrason. **SU-32**, 458–463 (1985).
12. A. M. Rollins, S. Yazdanfar, J. Barton, and J. Izatt, "Real-time in vivo color Doppler optical coherence tomography," J. Biomed. Opt. **7**, 123–129 (2002).
13. L. Hatle and B. Angelsen, Doppler Ultrasound in Cardiology (Lea & Febiger, Philadelphia, 1982).
14. B. Angelson, "Instantaneous frequency, mean frequency, and variance of mean frequency estimators for ultrasonic blood velocity Doppler signals," IEEE Trans. Biomed. Eng. **BME-28**, 733–741 (1981).
15. G. J. Tearney, B. E. Bouma, and J. G. Fujimoto, "High-speed phase- and group-delay scanning with a grating-based phase control delay line," Opt. Lett. **22, 23**, 1811–1813 (1997).
16. P. C. Li, C. J. Cheng, and C. K. Yeh, "On velocity estimation using speckle decorrelation," IEEE Trans. Ultrason. Ferroelectr. Freq. Control **48, 4**, 1084–1091 (2001).